5th Joint International Symposium on Deformation Monitoring (JISDM), 20-22 June 2022, Valencia, Spain
DOI: http://doi.org/10.4995/JISDM2022.2022.13728

Accuracy improvement of mobile laser scanning point clouds using graph-based trajectory optimization

Felix Esser, José Angel Moraga, Lasse Klingbeil, Heiner Kuhlmann

Institute of Geodesy and Geoinformation, University of Bonn, Nußallee 17, 53115 Bonn, Germany,
(esser@igg.uni-bonn.de; s7jomora@uni-bonn.de; l.klingbeil@igg.uni-bonn.de; heiner.kuhlmann@uni-bonn.de)

Key words: *point clouds; deformation analysis; mobile laser scanning; factor graph optimization; sensor fusion; GNSS/IMU processing*

ABSTRACT

The detection of deformations on man-made structures such as bridges and dams are an essential task in engineering geodesy. The classical method uncovering deformations is based on geodetic networks using measurements from total stations or GNSS receivers. Another new approach is the determination of deformations based on terrestrial laser scans leading to large-scale deformation results by point cloud comparisons. In the field of geodetic engineering, mobile laser scanning systems are increasingly used for high-resolution point cloud generation in short measurement times, which leads to the idea to use these for deformation analysis. A crucial part of this measurement strategy is the estimation of the trajectory (position and orientation) of the scanner, which allows a consistent registration of the single scan lines in a global coordinate system (georeferencing). The largest limitation to the accuracy of the resulting point cloud is the accuracy of the estimated trajectory. In most applications, the estimation of position and orientation are based on the fusion of GNSS (Global Navigation Satellite System) and IMU (Inertial Measurement Unit) measurements. Systematic errors, as they often appear in GNSS measurements, are directly transferred to the georeferenced point cloud and therefor limit the potential for deformation analysis. With this paper we address the questions, if the trajectory estimation can be improved by the integration of known landmarks into the trajectory estimation procedure. Using a point cloud generated with an initial GNSS/IMU based trajectory, landmark targets can be observed in the point cloud and integrated into an updated estimate, using a factor graph-based approach. For the evaluation of a potential accuracy increase due to landmark observations, we performed measurements, comparing GNSS/IMU based results with the ones where landmarks are additionally integrated. The experiments show, that the accuracy increases especially in the heading angle, which is reflected in lower residuals to observed reference coordinates, but also in the trajectory covariances of the estimation results.

I. INTRODUCTION

In recent years, the method of point cloud comparisons between consecutive epochs has become increasingly popular for detecting deformations of man-mad structures, such as bridges and dam walls (Neuner *et al.*, 2016; Xu *et al.*, 2018). The acquisition of these point clouds is usually realized by taking terrestrial laser scans from multiple points of view and then registering the individual scans into one. Another increasingly popular method for recording point clouds is the use of kinematic laser scanning with multi-sensor systems (MSS), (Heinz *et al.*, 2020; Eling *et al.*, 2015; Paffenholz, 2012). By estimating the position and orientation of the system for each laser observation in time, a georeferenced point cloud of the environment can be acquired. A crucial aspect in this procedure is a precise estimation of the trajectory.

An established method of trajectory estimation is the fusion of sensor information from GNSS (Global Navigation Satellite System) and IMU (Inertial Measurement Unit), where the accuracy of position and orientation depends significantly on the actual GNSS conditions. Systematic deviations in GNSS observations, caused by multipath and non-line of sight effects due to objects in the environment of the system (Zimmermann *et al.*, 2017; Strode and Groves, 2016), are directly transferred to the point cloud due to the direct georeferencing of the 2D scan profiles. This reduces the detectability of deformations in the context of deformation analysis. For this reason, it might be beneficial to include additional absolute sensor information in the trajectory estimation process, in order to reduce systematic errors in the trajectory and the resulting point cloud. This absolute sensor information can be obtained by observing known control points in the environment, either with a camera or with a laser scanner. In this work, we analyze the usage of a profile laser scanner, which is already part of the measurement system used in context of this work.

The integration of these observations introduces challenges for the algorithmic implementation. We chose a factor graph-based approach (Dellaert, 2012; Dellaert and Kaess, 2017; Choudhary *et al.*, 2015) for the integration of this information, which also realizes a smoothing of the trajectory. This approach is closely related to SLAM algorithms such as realized in Shan *et*

al., (2020) and Chang *et al.*, (2019). However, in contrast to most SLAM algorithms, we do not estimate the position of the landmarks within the process. Instead, we use the known positions to improve the estimate of the trajectory. The accuracy of the resulting point cloud (map) is improved in a second step.

We analysed the result of the method within an experiment, where we scanned an environment which contains a number of known landmark targets with our MSS. The evaluation of the accuracy improvement by observing and including landmark observations in the trajectory estimation is first performed by comparing the estimated variances of the trajectory states with and without inclusion of landmark information in the graph-based trajectory optimization algorithm. Furthermore, an evaluation of the residuals to landmark control points is performed. The rest of the paper is organized as follows: We first introduced the used sensor platform and the factor graph-based method for trajectory optimization in Section II, followed by the description of the experimental field used for evaluation. We discuss the evaluation results in Section III, closing this work by a conclusion and outlook in Section IV.

II. Materials and Methods

A. *Multi-Sensor System and Point Cloud Creation*

The multi-sensor system used in this study is well suited for mobile laser scanning in urban areas and consists of a high-end Inertial Navigation System (INS) (IMAR iNav-FJI-SURV), a GNSS antenna (Leica AS10) and a high-precision profile laser scanner (Z+F Profiler 9012A), see Figure 1, left. In a measurement campaign, the system can be fixed to the roof of a vehicle. In order to exclude the vehicle from the field of view of the sensor, the scanner is tilted by 30°.

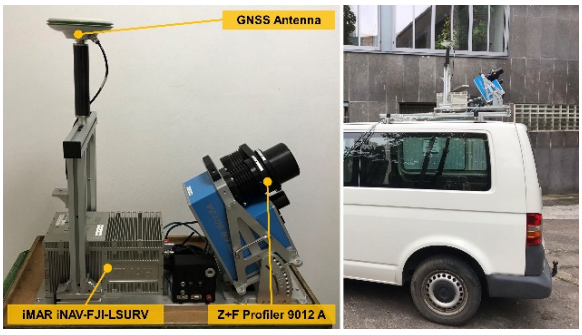

Figure 1. Multi-Sensor System with GNSS Antenna, IMU with integrated GNSS receiver and profile laser scanner. *Right*: MSS mounted on vehicle.

The INS consist of an internal multi GNSS receiver, a fiber optic gyroscope and servo accelerometers in all three spatial axes. Data can be recorded with a rate of up to 1500 kHz. The integrated Novatel OEM628 Multi GNSS receiver provides centimeter accurate position estimates using kinematic baseline processing.

The Z+F profile laser scanner delivers up to 1 million points per second with a spatial resolution of 0.5 mm at a distance of 3 m, and a distance accuracy of less than 1 mm, as specified by the manufacturer. The scans are synchronized to the INS data using the PPS (Pule-Per-Second) signal from the GNSS receiver.

In order to create a georeferenced point cloud, the laser scans have to be transformed using the georeferencing equation (Eq. 1):

$$\begin{bmatrix} x_g \\ y_g \\ z_g \end{bmatrix} = \begin{bmatrix} t_x \\ t_y \\ t_z \end{bmatrix} + \mathbf{R}_n^e(\theta,\psi,\phi)\left[\begin{bmatrix} \Delta x \\ \Delta y \\ \Delta z \end{bmatrix} + \mathbf{R}_s^b(\alpha,\beta,\gamma)\begin{bmatrix} x_s \\ y_s \\ z_s \end{bmatrix}\right] \quad (1)$$

The laser measurements $[x_s, y_s, z_s]$ given in the sensor frame of the scanner are transformed into the body frame *b* using the system calibration parameters, which are the translation vector $[\Delta x, \Delta y, \Delta z]^T$ and the rotation matrix $\mathbf{R}_s^b$. The subsequent transformation from the body into the global frame g requires the estimation of the trajectory parameters, which are the positions $[t_x, t_y, t_z]^T$ and orientations $\mathbf{R}_n^e$ (or roll, pitch and yaw angles θ, ψ and ϕ) for each laser scanner measurement. The determination of these parameters is the main contribution in this study and will be described later.

Apart from the position and orientation states, the system calibration parameters also have a significant influence on the accuracy of the resulting point cloud. We estimated them very accurately using a plane-based approach which is described in more detail in (Heinz *et al.*, 2015).

B. *Measurements and State Definition for Trajectory Optimization*

The calculation of the trajectory is based on the measured rotation rates and accelerations of the IMU, the GNSS position information processed from the baseline and the laser measurements of the profile scanner to the known landmark coordinates.

1) GNSS: In the trajectory estimation a loosely coupled approach is used for the integration of the GNSS information. For this reason, we performed a kinematic GNSS carrier-phase based baseline processing, using a virtual reference station from *SAPOS NRW*. The GNSS coordinates for each GNSS epoch *j* are given by $\mathbf{z}_j^{GNSS} = \{x, y, z\}_j$ with a corresponding standard deviation.

2) Landmark Targets: In order to create target observations, we first compute the initial point cloud based on the trajectory estimation with GNSS and IMU observations only. In this point cloud the known landmark targets are visible which allows to manually deduce the laser scanner observation to the target centrum. The detection of the target center and corresponding observation could also be performed automatically, but is beyond the scope of this paper.

The laser observations of the target centers are first given in the sensor frame in cartesian coordinates, and then transformed into the body frame using the system calibration parameters, and finally converted into polar coordinates. This results in two angles and a distance measurement, which are called bearing φ, θ and range d. The full set of observations to n landmarks is given by $\mathbf{z}_n^{BR} = \{\varphi, \theta, d\}_n$. An example target resolved in the initial point cloud is visualized in Figure 2.

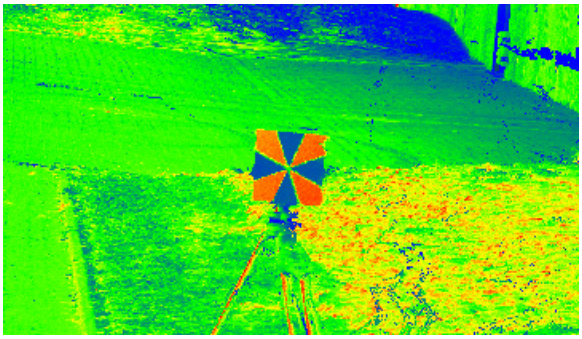

Figure 2. Example landmark target in initial point cloud, computed with GNSS / IMU trajectory.

3) IMU: The measured accelerations a and angular velocities ω of the IMU $\mathbf{z}_l^{IMU} = \{a_x, a_y, a_z, \omega_x, \omega_y, \omega_z\}_l$ are given in the IMU frame which coincides with the body frame of the system and therefore do not have to be transformed.

All sensor observations can be summarized in the set $M = \{\mathbf{z}_j^{GNSS}, \mathbf{z}_l^{IMU}, \mathbf{z}_n^{BR}\}$ marked with the corresponding indices to distinguish between different sensor observations.

4) States: The state vector describing position, velocity and orientation of the system, defining one navigation system state in time, is given by $\mathbf{x_i} = [x, y, z, v_x, v_y, v_z, \boldsymbol{q}_{rpy}]_i^T$.

The position coordinates x, y, z, velocities v_x, v_y, v_z and orientation $\boldsymbol{q}_{rpy}$ refer to the UTM (Universal Transverse Mercator) coordinate system in which the estimation of the states is implemented. The description of the orientation angles roll, pitch and yaw are represented by the quaternion $\boldsymbol{q}_{rpy}$ and refers to the axes of the navigation frame, coinciding with the axes of UTM. Due to the dynamic evolution of the IMU bias in time (Groves, 2015), it is necessary to include inertial sensor bias variables in the optimization in order to remove the systematic errors from the raw IMU observations. The additional six parameters for the IMU bias result in $\mathbf{b}_q = [v_x, v_y, v_z, v_x, v_y, v_z]_q^T$.

Summarizing the trajectory states and bias variables over the entire measurement period k, all states to be optimized result in $\mathbf{v}_k = \{\{\mathbf{x_i}\}\{\mathbf{b_q}\}\}$.

Since the landmark coordinates are available with very high accuracy, they are assumed to be known and are therefore not included as optimizing quantities in the set of state vectors $\mathbf{v}_k$.

C. *Factor Graph-Based State Optimization*

We use a factor graph-based approach to optimize the trajectory state variables $\mathbf{v}_k$. Within the graph, nodes describe the states to be estimated. The sensor observations result in so-called factors, which contain sensor observations and state variables. By assuming zero mean gaussian noise for the sensor measurements, the factors represent error functions involving measurements and variables. The factor graph representation of variables nodes and factors for the estimation problem in this work is visualized in Figure 3. More information about concept and definitions of factors is given in (Kaess *et al.*, 2012). We introduce first the least squares optimization problem containing factors and state variables. Afterwards we define the individual factors and their error functions.

1) Least Squares Optimization: By setting up all error functions over the entire period for sensor measurements and defining the variable nodes, the optimization of all trajectory states can be described by the least squares problem (Eq. 2)

$$\mathbf{v}_k^* = \arg min_{X_k} \sum_j \|f^{IMU}\|^2_{\Sigma^2_{\Delta\Delta}} + \sum_j \|f^{BIAS}\|^2_{\Sigma^2_{cc}} + \sum_j \|f^{GNSS}\|^2_{\Sigma^2_{xx}} + \sum_j \|f^{GNSS}\|^2_{\Sigma^2_{xx}} \quad (2)$$

assuming zero mean gaussian noise for all sensor observations. The corresponding factor graph visualization to Equation 2 is visualized in Figure 3 and is composed of the individual factors, that we introduce in the following.

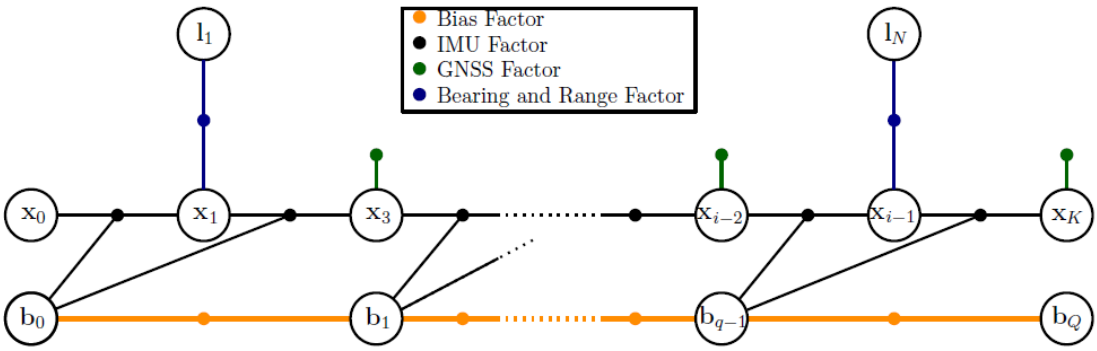

Figure 3. Full factor graph representation of the least squares problem (Equation 2).

By linearizing the individual error functions of the graph by a first order Taylor expansion, the normal equations can be set up containing all navigation states $\mathbf{x}$ and IMU bias states $\mathbf{b}$. The linearization requires knowledge about approximate values for each variable node of the graph to be optimized. These are not available for the orientation parameters, since these must be updated in time by integrating the IMU observations. To solve this problem, we use the ISAM2 algorithm that incrementally builds up the graph structure and optimizes the state variables periodically in time. The algorithm is implemented in the GTSAM library, detailed information about library and ISAM2 algorithm used for optimizing the graph can be found in (Kaess *et al.*, 2011; 2012; Indelman *et al.*, 2013).

2) Preintegrated IMU Factor: The IMU factor is a non-linear error function involving two consecutive navigation states in time $\mathbf{x}_{i-1}$ and $\mathbf{x}_i$, and the corresponding bias states $\mathbf{b}_q$ and is defined by (Eq. 3)

$$f^{IMU}(\mathbf{x}_{i-1}, \mathbf{x}_i, \mathbf{b}_q) = err^{IMU}\left(\mathbf{x}_i - h(\mathbf{x}_{i-1}, \mathbf{b}_q, \mathbf{\Delta x}_{i-1\rightarrow i})\right). \quad (3)$$

By preintegrating the raw IMU observations considering the estimated bias variables $\mathbf{b}_q$, the so-called preintegrated IMU measurements $\mathbf{\Delta x}_{i-1\rightarrow i}$, related to the time interval between two defined navigation states $\mathbf{x_i}$ and $\mathbf{x_{i-1}}$ are obtained. The factor calculates the error of the current state $\mathbf{x}_i$ and the predicted state by the function $\boldsymbol{h}()$ involving the previous state, bias state and preintegrated measurements and is minimized in the least-squares optimization. More information about the preintegration, including the bias variables is given in Forster (2015).

3) IMU Bias Factor: The evolution of the bias variables requires a model for propagation in time which is computed by a function $g(\mathbf{b}_{q-1})$ assuming a zero-mean gaussian noise model. By the definition of this noise model with a random walk process, the bias factor results in (Eq. 4)

$$f^{BIAS}(\mathbf{b}_q, \mathbf{b}_{q-1}) = d(\mathbf{b}_q - g(\mathbf{b}_{q-1})) \quad (4)$$

The error function computes the residuals of predicted bias by $g(\mathbf{b}_{q-1})$ and current bias state $\mathbf{b}_q$, minimized in the optimization. More information about the bias factor and the connection to the preintegrated IMU factor is given in (Forster *et al.*, 2016).

4) GNSS Factor: The GNSS factor is a so-called unary factor and is defined by the linear error function (Eq. 5)

$$f^{GNSS}(\mathbf{x}_j) = err^{GNSS}\left(\mathbf{z}_j^{GNSS} - h^{GNSS}(\mathbf{x}_j)\right) \quad (5)$$

which computes the error between the GNSS position measurement $\mathbf{z}_j^{GNSS}$ and predicted position by the function $h^{GNSS}(\mathbf{x}_j)$ including the navigation state $\mathbf{x}_j$ and the translation from body to GNSS antenna frame, the so-called lever arm.

5) Bearing and Range Factor: The bearing and range factor is described by the error function (Eq. 6)

$$f^{BR}(\mathbf{x}_i) = err^{BR}(\mathbf{z}_n^{BR} - \pi^{BR}(\mathbf{x}_i, \mathbf{l}_n)) \quad (6)$$

computing the error between predicted bearing and range measurement by the function π^{BR} depending on the current trajectory state $\mathbf{x}_i$, known landmark $\mathbf{l}_n$ and laser scanner measurement $\mathbf{z}_n^{BR}$. Detailed information about the bearing and range factor is given by (Setterfield *et al.*, 2017; Dellaert, 2012).

6) Sensor Noise Models: The weighting of the sensor information within the optimization of the state variables requires the definition of noise models for the factors in Figure 2, in which the observations are included. The specified standard deviations of the individual observations, which we used for the optimization are collected in Table 1. The standard deviation of the target measurements in Table 1 refer to the coordinates in the sensor frame of the laser scanner. The standard deviations of bearing and range in the body frame are determined by a variance propagation considering the accuracy of the system calibration. The variances of the raw IMU observations are also transferred to the preintegrated IMU observations of the IMU factor by a variance propagation (Forster *et al.*, 2015).

Table 1. Sensor noise models for the individual measurements

GNSS	IMU and Bias		Target
$\sigma_x, \sigma_y, \sigma_z$ 5cm	Acceleration $\sigma_{ax}, \sigma_{ay}, \sigma_{az}$ $7.8 \cdot 10^{-5}\ m/s$ Bias noise $7 \cdot 10^{-5}\ m/s$	Gyroscope $\sigma_{\omega x}, \sigma_{\omega y}, \sigma_{\omega z}$ $3 \cdot 10^{-7}\ rad/s$ Bias noise $5 \cdot 10^{-7}\ rad/s$	$\sigma_x^l,\ \sigma_y^l,\ \sigma_z^l$ 5mm

D. *Experimental Setup for Evaluation*

For recording measurements and later evaluation of our results we use an existing experimental field 20 km in west of the city of Bonn, Germany. We perform a network adjustment based on total station observations and static GNSS measurements to optimize a geodetic net with points known with an accuracy in submillimeter range in global frame.

A subset of these coordinates was used as reference coordinates for evaluation purposes, while another subset was used as observations in the trajectory estimation process. In order to transform the local network into the UTM frame, known datum points are observed which are available with a high accuracy near the location of the network. By performing a least squares network adjustment, considering the datum

information, the network point coordinates are estimated with a standard deviation below 1 mm. The distribution of network points and points defining the datum are visualized in Figure 4.

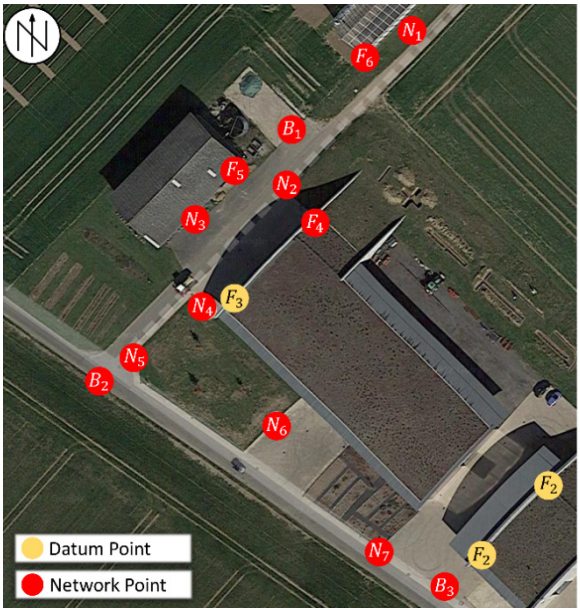

Figure 4. Resulting coordinates from network adjustment (Image Source: Google Maps, 2022).

We perform multiple measurement drives with the car setup shown in Figure 1. The start and end points of campaigns are located in the north of the measurement area and proceeds through the geodetic network in the middle part. To ensure a high resolution of the landmark targets in the point cloud, a low velocity of the system near the landmarks of only about 10 cm/s is chosen. An example target is visualized in Figure 2.

We perform two trajectory optimizations: The first on basis of GNSS and IMU observations only and the second with additional landmark observations, in order to elaborate the accuracy improvement due to target observations. The analysis focusses on comparison of both trajectories regarding the precision gain of position and orientation. Highlighting the influence of the bearing and range factors on state estimation in more detail, the number of GNSS observations within the algorithm is reduced by the factor 20 resulting in a GNSS position update rate of 10 s. Afterwards we analyze the residuals to the subset of coordinates from the geodetic network that we did not include in the trajectory optimization.

III. Results and Discussion

A. *Trajectory Estimates*

Figure 5 shows an example trajectory estimate with included landmark observations in the trajectory estimation.

We use the target measurements to the red network points in Figure 5 to formulate the bearing and range factors, include them in the factor graph and perform the trajectory optimization. The factors are visualized in Figure 5 as red lines connecting landmark target and corresponding trajectory state. The subsequent discussions are made on basis of the chosen trajectory part introduced within this section.

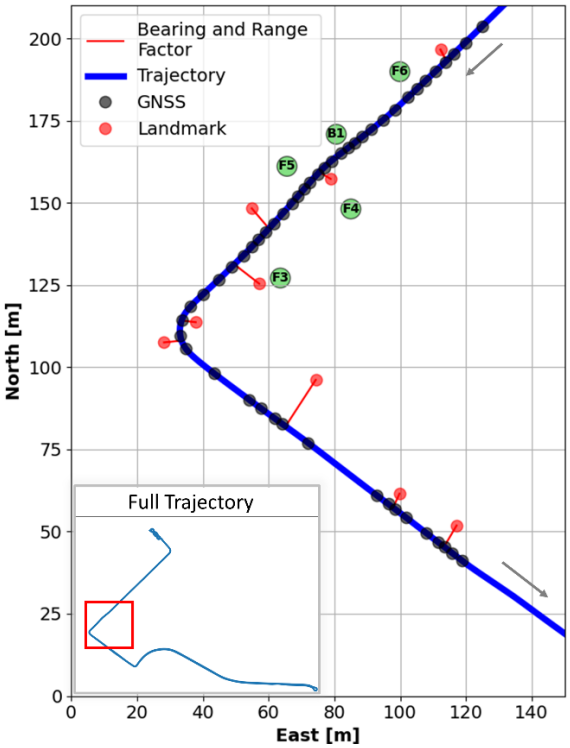

Figure 5. Trajectory state of east and north coordinate (blue), GNSS observations (black, rate: 10 s) and landmarks. Bearing and range factors (red lines) connect landmark and corresponding trajectory states.

B. *Estimate of Trajectory Variances*

The ISAM2 algorithm also provides estimated covariance information for the trajectory states, which allows the evaluation of the precision gain when including the landmark observations. For the analysis we compare the variances of the estimates based on GNSS and IMU measurements only and with the ones where additional target observations are included. The time interval of occurring landmarks and estimated standard deviations of the orientation angles roll, pitch and yaw is visualized in Figure 6. This selected interval corresponds to the trajectory part shown in Figure 5. The yaw angle is clearly improved in precision by about 50% (~0.5°) over the whole section compared to the estimation without landmark information. The precision of pitch and roll angle is also improved, but less significant (0.01° –0.02°). Overall, this improvement has not only a positive effect close to the target observations, but also in between of two of them. The overall higher standard deviations in the yaw angle in both estimates compared to roll and pitch can be explained by the non-eccentric mounting of the GNSS antenna, which prevents an indirect observation of the yaw angle by the GNSS positions, resulting in higher standard deviation estimates for yaw.

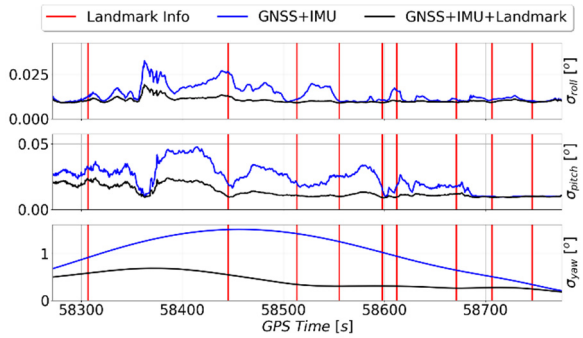

Figure 6. Estimated orientation standard deviations of roll, pitch and yaw angles, GNSS + IMU vs. GNSS + IMU + Landmark. The time interval visualized corresponds to the trajectory section from figure 5. Red lines mark times of landmark observations.

Figure 7 shows for the corresponding time interval for the estimated position standard deviations of the trajectories with and without landmark information. A GNSS position update has been used in the graph every 10 seconds.

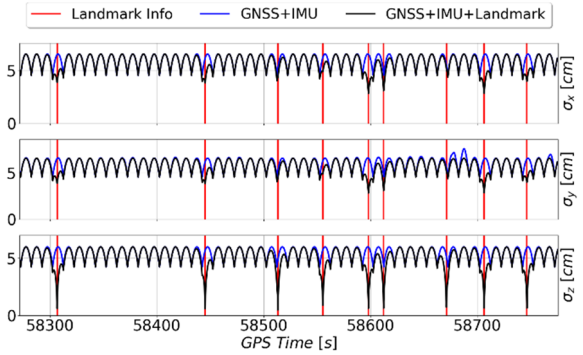

Figure 7. Estimated position standard deviations (X=east, Y=north, Z=height), GNSS + IMU vs. GNSS + IMU + Landmark. The time interval shown corresponds to the trajectory section from figure 4. Red lines mark times of landmark observations.

The arc-like increase of the standard deviations in the position in all three coordinates between two GNSS observations can be explained by the relative propagation of the variances in the IMU preintegration and is about 6 cm in the middle between two GNSS positions. GNSS coordinates are included in the estimation with a standard deviation of 5 cm which indicates a reliable variance propagation of the preintegrated IMU factor.

At the time of landmark observations, the standard deviations can be significantly decreased by about 1-2 cm in east (X) and north (Y). In the ellipsoidal height (Z) a reduction of the standard deviation to about 1 cm can be observed, see Figure 7. Compared to the precision increase of the orientation angles, the observations of landmark targets cause only a local improvement of the precision.

C. *Root Mean Squared Error*

So far, we focused entirely on the increase in precision by comparing the variance estimates. In order to be able to make a statement about the point accuracy of MSS, the green reference points shown in Figure 5 are used, known with a standard deviation in the sub-millimeter range due to the network adjustment.

Using the georeferencing Equation 1, the laser scanner measurements to reference points are transformed to the UTM coordinate frame, resulting in the target center coordinates. For evaluation of the increase in accuracy, we analyze the residuals to the reference coordinates. The residuals computed with the trajectory based on GNSS and IMU measurements only and with included bearing and range factors are compared to each other.

In order to visualize the accuracy improvement due to the integration of landmark information, several trajectory estimates are performed with a decreasing number of GNSS position data in the trajectory estimation. For each estimate, the root mean squared error (RMSE) to the reference coordinates is calculated, which is defined by (Eq. 7)

$$RMSE_x = \sqrt{\frac{\sum_{i=0}^{N} (\hat{x} - x)^2}{N}} \qquad (7)$$

in which x describes the coordinate estimated from the sensor system with the corresponding trajectory estimate and $\hat{x}$ marks the reference coordinate from the network adjustment. The number of reference points used for RMSE computation is marked by N.

The results of the RMSE values are shown in Figure 8 for the east, north and ellipsoidal height for one measurement drive. For evaluation we performed several estimation runs and incrementally increased the time between consecutive GNSS position updates from 1 to 50 seconds.

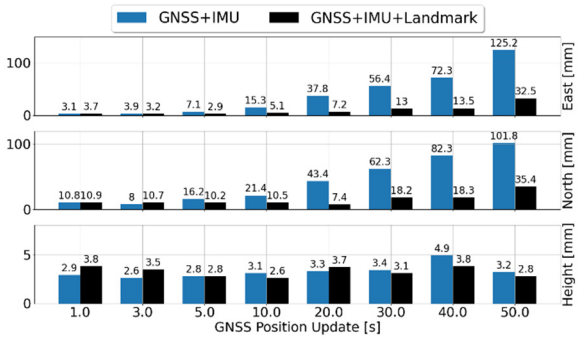

Figure 8. Root mean squared error of georeferenced control points from MSS and reference coordinates from network adjustment (Figure 5, green points). GNSS + IMU *vs. GNSS + IMU + Landmark.*

Comparing the RMSE values for the coordinates computed with both trajectory estimates in Figure 8 significant differences are observable. The reduction of the height RMSE when inserting landmark information is the smallest with just a few mm and can be considered as barely significant, comparing the RMSE to the estimate without landmark information. A possible reason for this non-significant influence could be the much higher accuracy in the states of the roll and pitch angles, see Figure 6.

In contrast to this observation, we see an increase in RMSE in the X, Y coordinates (north and east), especially detectable when inserting less GNSS position updates in the trajectory estimation. Comparing both estimates at a GNSS position update rate of 30 s the east RMSE can be reduced by about 40 mm, in north a reduction of over 45 mm is visible, when target observations are included into the state optimization, see Figure 8.

The significant increase can be explained by the lower yaw angle precision compared to pitch and roll, see Figure 6. Errors in the yaw angle are directly transferred to the east and north coordinates, resulting in higher errors in these coordinates, when computing the RMSE to the reference coordinates. Please note, that the result only shows one particular measurement and that the maximal achieved accuracy may vary, depending on the GNSS conditions at the particular time and location of this measurement.

IV. Summary and outlook

Using the graph-based approach of trajectory estimation, landmark information can be easily incorporated as bearing and range factor in the trajectory estimation.

The analysis of the accuracy gains by including landmark target information have shown a significant improvement of the yaw angle precision. A significant increase in roll and pitch angle accuracy could not be demonstrated. Improvements in position coordinates have only local effect compared to improvements of the angle variance estimates.

The analysis of the root mean squared error when comparing to known reference coordinates results in lower values for the east and north coordinates, but not for the height residuals. This is especially valid when the number of GNSS observations are decreased in the trajectory estimation procedure.

With this study we showed, that it can be beneficial for the accuracy of the trajectory estimation of a mobile mapping system, when additional information from known landmarks are included into the estimation. This is especially valid, when GNSS observations are less often available. We also presented a procedure how this can be realized, using a graph-based optimization approach. As the trajectory accuracy directly transfers to the accuracy of the resulting point cloud we can assume, that deformations can be better detected. In an extension of the work, we will evaluate the resulting point cloud using reference information.

V. Acknowledgements

Funding: This work was funded by the Deutsche Forschungsgemeinschaft (DFG, German Research Foundation) under Germany's Excellence Strategy–EXC 2070–390732324.

References

Chang, L., Niu, X., Liu, T., Tang, J., and Qian, C. (2019). GNSS/INS/LiDAR-SLAM integrated navigation system based on graph optimization. *Remote Sensing*, 11(9), 1009.

Choudhary, S., Indelman, V., Christensen, H. I., and Dellaert, F. (2015, May). Information-based reduced landmark SLAM. In 2015 IEEE International *Conference on Robotics and Automation* (ICRA) (pp. 4620-4627). IEEE.

Dellaert, F. (2012). *Factor graphs and GTSAM: A hands-on introduction*. *Georgia Institute of Technology*.

Dellaert, F., and Kaess, M. (2017). Factor graphs for robot perception. *Foundations and Trends® in Robotics*, 6(1-2), pp. 1-139.

Eling, C., Klingbeil, L., and Kuhlmann, H. (2015). A direct georeferencing system for real-time position and attitude determination of lightweight UAVs. In *FIG Working Week*.

Forster, C., Carlone, L., Dellaert, F., and Scaramuzza, D. (2016). On-manifold preintegration for real-time visual--inertial odometry. *IEEE Transactions on Robotics*, 33(1), pp. 1-21.

Forster, C., Carlone, L., Dellaert, F., and Scaramuzza, D. (2015). On-manifold preintegration theory for fast and accurate visual-inertial navigation. IEEE Transactions on Robotics, 1-18.

Groves, P. D. (2015). Principles of GNSS, inertial, and multisensor integrated navigation systems, [Book review]. IEEE Aerospace and Electronic Systems Magazine, 30(2), pp. 26-27.

Heinz, E., Eling, C., Wieland, M., Klingbeil, L., and Kuhlmann, H. (2015). Development, calibration and evaluation of a portable and direct georeferenced laser scanning system for kinematic 3D mapping. *Journal of Applied Geodesy*, 9(4), pp. 227-243.

Heinz, E., Eling, C., Klingbeil, L., and Kuhlmann, H. (2020). On the applicability of a scan-based mobile mapping system for monitoring the planarity and subsidence of road surfaces–Pilot study on the A44n motorway in Germany. *Journal of Applied Geodesy*, 14(1), pp. 39-54.

Indelman, V., Williams, S., Kaess, M., and Dellaert, F. (2013). Information fusion in navigation systems via factor graph based incremental smoothing. *Robotics and Autonomous Systems*, 61(8), pp. 721-738.

Kaess, M., Johannsson, H., Roberts, R., Ila, V., Leonard, J., and Dellaert, F. (2011, May). iSAM2: Incremental smoothing and mapping with fluid relinearization and incremental variable reordering. In *2011 IEEE International Conference on Robotics and Automation* (pp. 3281-3288). IEEE.

Kaess, M., Johannsson, H., Roberts, R., Ila, V., Leonard, J. J., and Dellaert, F. (2012). iSAM2: Incremental smoothing and mapping using the Bayes tree. *The International Journal of Robotics Research*, 31(2), pp. 216-235.

Neuner, H., Holst, C., and Kuhlmann, H. (2016). Overview on current modelling strategies of point clouds for deformation analysis. *Allgemeine Vermessungs-Nachrichten: AVN; Zeitschrift für alle Bereiche der Geodäsie und Geoinformation*, 123(11-12), pp. 328-339.

Paffenholz, J. A. (2012). *Direct geo-referencing of 3D point clouds with 3D positioning sensors* (Doctoral dissertation, Hannover: Gottfried Wilhelm Leibniz Universität Hannover).

Setterfield, T. P., Miller, D., Leonard, J. J., and Saenz-Otero, A. (2017, March). Smoothing-based estimation of an inspector satellite trajectory relative to a passive object. In *2017 IEEE Aerospace Conference* (pp. 1-11). IEEE.

Shan, T., Englot, B., Meyers, D., Wang, W., Ratti, C., and Rus, D. (2020, October). Lio-sam: Tightly-coupled lidar inertial odometry via smoothing and mapping. In *2020 IEEE/RSJ international conference on intelligent robots and systems (IROS)* (pp. 5135-5142). IEEE.

Strode, P. R., and Groves, P. D. (2016). GNSS multipath detection using three-frequency signal-to-noise measurements. *GPS solutions*, 20(3), pp. 399-412.

Xu, X., Bureick, J., Yang, H., and Neumann, I. (2018). TLS-based composite structure deformation analysis validated with laser tracker. *Composite Structures*, 202, pp. 60-65.

Zimmermann, F., Eling, C., and Kuhlmann, H. (2017). Empirical assessment of obstruction adaptive elevation masks to mitigate site-dependent effects. *GPS Solutions*, 21(4), pp. 1695-1706.